Geophysical Journal International

Geophys. J. Int. (2014) **198,** 1208–1221 doi: 10.1093/gji/ggu184
GJI Geomagnetism, rock magnetism and palaeomagnetism

New directional archaeomagnetic data of burned cave sediments from Switzerland and geomagnetic field variations in Central Europe

K. L. Kapper,[1] F. Donadini,[1] M. Mauvilly,[2] S. Panovska[3] and A. M. Hirt[1]

[1]*Institute of Geophysics, ETH Zurich, Switzerland. E-mail: klkapper@gmail.com*
[2]*Amt für Archäologie, Fribourg, Switzerland*
[3]*Institute of Geophysics and Planetary Physics, Scripps Institution of Oceanography, University of California, San Diego, CA 92093-0225, USA*

Accepted 2014 May 16. Received 2014 May 9; in original form 2013 August 21

SUMMARY

This paper presents new directional archaeomagnetic data from nine Meso-/Neolithic fireplaces, sampled in a cave shelter, at Arconciel, in western Switzerland. Rock magnetic measurements indicate a homogenous magnetic mineralogy in all fireplaces, with magnetite as the main magnetic carrier. The remanent magnetization is stable and generally shows one characteristic directional component. Nine new directions, which were obtained from Arconciel, are combined with 356 other archaeomagnetic data from a circular area with a radius of 700 km around this site, to obtain a penalized least square spline fit for the past 9000 yr. We found in general good agreement with other local compilations, such as the Balkan curve, the regional SCHA.DIF.8k model and with lake sediments from UK, Fennoscandia and Switzerland. Nevertheless, a time lag of several centuries is observed for a declination maximum between the archaeomagnetic spline fit and the other European data records around 5900 BC. This time lag is also observed in the Swiss lake sediment record; therefore we interpret this shift as a local feature of the Earth's magnetic field.

Key words: Palaeomagnetic secular variation; Rock and mineral magnetism; Europe.

1 INTRODUCTION

Systematic observations of the geomagnetic field are available for the last two centuries coming from geomagnetic observatory and ship data, as well as satellites for the last 50 yr (e.g. Jackson *et al.* 2000; Olsen & Stolle 2012). These data have been used to accurately model the main dipole field but also the non-dipole contributions, which show features such as the South Atlantic anomaly (e.g. Pinto Jr *et al.* 1992, for a review) and the equatorial flux spots (Jackson 2003). The temporal change of the geomagnetic field in direction and intensity is referred to as secular variation. Crucial for any model of secular variation of the past field is high quality palaeomagnetic information, which mainly comes from archaeomagnetic and lake sediment data. Holocene geomagnetic field models such as CALS10k.1b (Korte *et al.* 2011) or SCHA.DIF.8k (Pavón-Carrasco *et al.* 2010) mainly rely on lake sediment data for time periods earlier than 1000 BC. Lake sediments cover long time periods, however, their relatively large scatter, which is due to inconsistent lake sediment records, is responsible for strong smoothing of the CALS10k.1b (Korte *et al.* 2011). They often carry a post-depositional remanent magnetization, which is acquired some time after their deposition when the magnetization is locked in (e.g. Verosub 1997). The lock-in depth is related to sedimentation rate and composition (Bleil & von Dobeneck 1999), and is generally considered to be around 10 cm depth (e.g. Roberts & Winklhofer 2004). Therefore, there is a time lag between the age of the sediment and its magnetization, which causes smoothing of the magnetization signal when averaging over time (e.g. Roberts & Winklhofer 2004; Panovska *et al.* 2012). In contrast, archaeological artefacts have been shown to be faithfull recorders of the Holocene geomagnetic field, particularly for the last 3000 yr (*cf.* Donadini *et al.* 2010; Pavón-Carrasco *et al.* 2010). Data coming from burned archaeological structures and burned sediments are temporarily better constrained in capturing the geomagnetic field. The thermoremanent magnetization in these materials was acquired during the last burning event. The magnetization of the unburned material is considerably enhanced through burning, because weakly magnetic oxides and hydroxides as well as non-magnetic minerals are transformed into stronger ferrimagnetic phases, for example magnetite or maghemite (Le Borgne 1955; McClean & Kean 1993; Canti & Lindford 2000). More recently, Carrancho *et al.* (2009) showed that burned Neolithic sediments (fumiers) carry a stable remanent magnetization, related to the burning process. Carrancho & Villalaín (2011) quantified the magnetic enhancement on experimental hearths to illustrate the potential of these structures to acquire robust geomagnetic field data. Burned sediments are particularly valuable because they can provide information on field behaviour prior to 1000 BC, where there is a paucity of data.

In this study, we present directional data from nine ancient fireplaces excavated at the Arconciel/La Souche shelter to reconstruct the geomagnetic field. The data cover a time period from approximately 4500–6800 cal. BC. Common rock magnetic measurements were performed to investigate the magnetic mineralogy and grain sizes of the studied samples, as well as the stability of their natural remanent magnetization. We take advantage of the stratification of burned sediments to construct an age model using the available ^{14}C dates. We combine this new data with high-quality data from the Geomagia50 v.2 database (Donadini *et al.* 2006; Korhonen *et al.* 2008) and recently published archaeomagnetic data from northern Italy (Kapper *et al.* 2014), in order to establish a penalized least squares spline fit (Constable & Parker 1988; Panovska *et al.* 2012). This new data compilation is compared to global and regional models, to other archaeomagnetic data from the Balkan region (Tema & Kondopoulou 2011), and to lake sediment records.

2 SITE PRESENTATION AND FIELD WORK

2.1 Formation of the rock shelter

The Arconciel/La Souche rock shelter (ARC; latitude 46.76°N and longitude 7.11°E) is situated about 4 km south of the city of Fribourg (Switzerland), on the right bank of a large meander in the Sarine river (Fig. 1). The shelter is located at the base of a sandstone cliff, just above the prehistoric water level. The shelter is 5–6 m deep and about 50 m long. Between 2003 and 2012, the northwestern area of the shelter, corresponding to about 40 m^2, was excavated during 10 field campaigns. The excavations revealed deposits ranging between 4 and 6 m in thickness, depending on the amount of erosion from the roof of the shelter. These deposits were ^{14}C-dated and cover ages between 7000 and 4900 BC. This time period corresponds to the entire late Mesolithic and the beginning of the Neolithic. The layers include a large number of anthropogenic artefacts, and the continuity of the deposits and the abundance of hearths indicate frequent use of the shelter for domestic purposes. The finding of the pintadera, a prehistoric stamp (Mauvilly *et al.* 2008b), suggests that the culture had contact or exchange with the Mediterranean region.

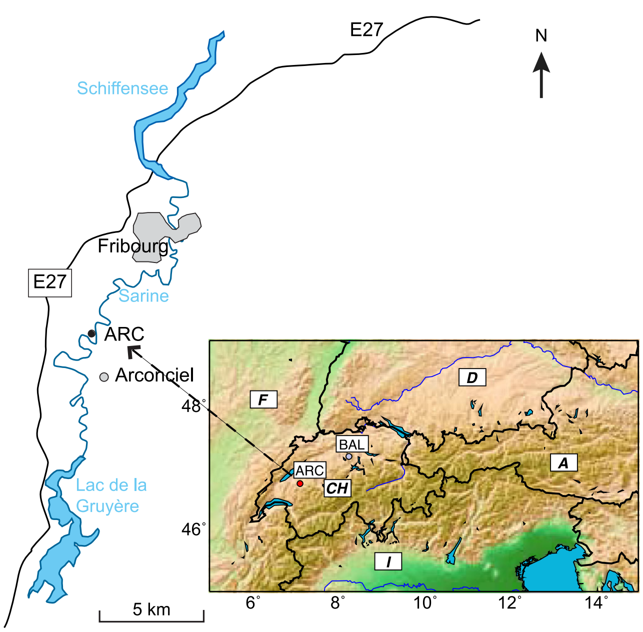

Figure 1. Map showing the location of the excavation site of Arconciel (ARC), Fribourg (Switzerland). The location of Lake Baldegg (BAL) is also indicated. CH, Switzerland; F, France; I, Italy; A, Austria; D, Germany.

Fig. 2(a) shows a schematic picture of the shelter, which is characterized by six archaeological units. These units are defined by the type of archaeological material and sediment found in the unit, and chronostratigraphic information. Further, each unit consists of various layers, showing a clear stratigraphic succession. The variety of archaeological artefacts shows the evolution of the cultures living in the area surrounding the ARC shelter during this period. For example, trapezoidal armature, a lithic tool, evolved from a very thin and narrow shape to larger ones, which define the boundary between Units VI and V. These were then succeeded by more advanced armatures made by inverse plain retouche technique (Nielsen 2009), which marks the transition from Unit IV to III at ARC shelter. The evolution of the debitage, that is, small flakes removed during lithic production, is a further indicator of a change in lithic manufacturing techniques. For example, bladelets became long and more regular at the boundary between Units III and IV and agree with the above mentioned armature change (Mauvilly *et al.* 2008a). Based on the sedimentological and the archaeological analyses the occupation of the shelter between 6750 and 6530 BC (Unit VI) was sometimes hampered by flooding events of the Sarine river. Starting from Unit V (6600 BC) the periods of abandonment become more sporadic and the shelter appears to be frequented on a regular basis. The rather fast sedimentation rate occurring during this period probably lead to a reduced living space, and so around 5800 BC (Unit III) the visits to the shelter appear to decrease systematically.

The archaeological excavation uncovered about 60 fireplaces (FA) in total, which can be easily distinguished from each other thanks to the presence of sand layers between the structures. The large number of undisturbed structures associated with these layers makes the shelter an ideal location to study the geomagnetic field evolution during the Meso-Neolithic in Switzerland. Fireplaces that were investigated at ARC are shown in Fig. 2(a). A photo, which illustrates the stratigraphic succession of fireplaces FA40 to FA32A is shown in Fig. 2(b). In this succession samples were collected horizontally. Fig. 2(c) shows fireplace FA32A, which was sampled vertically. The function and use of these layers and hearths, and their connection to the behaviour of the cultures using them, is presently under investigation by the archaeologists at the Amt für Archäologie, Fribourg (Switzerland). The inclination of the layers did not occur after their deposition, but is related to the use of the fireplaces. In the upper Units II and III fireplaces are better visible within the stratigraphy because they show a well rubefied sediment section. The fireplaces consist either of ash or burned soil (silt and sand). The larger fire pits, which were used over a long period of time (e.g. FA32), consist of a succession of different layers (carbonaceous, ash and burned soil). In particular, FA32 consists of a sequence of three individual fireplaces: FA32-1, FA32-2 and FA32-5. The chance of partial reheating of these successions of fireplaces is assumed to be rather low, because temperature decreases very rapidly with depth. For example, Carrancho & Villalaín (2011) showed that temperatures in the centre of an experimental fire do not exceed 245°C in 3–4 cm depth. Fireplaces located in the lower part of the shelter (Units IV and V) mainly consist of ash. The diametre of the fire pits can measure up to several metres and can be grouped into essentially two main shapes: flat–type and basin-type. One distinctive feature of this site is the thickness of the ash layers in Unit IV, which can often reach 10–15 cm over a surface of 4 m^2. The layers are well preserved in general, but animals may have disturbed the site in a few places. It is presumed that the ashes were used to level the ground, particularly after the last use of the basin-type hearths.

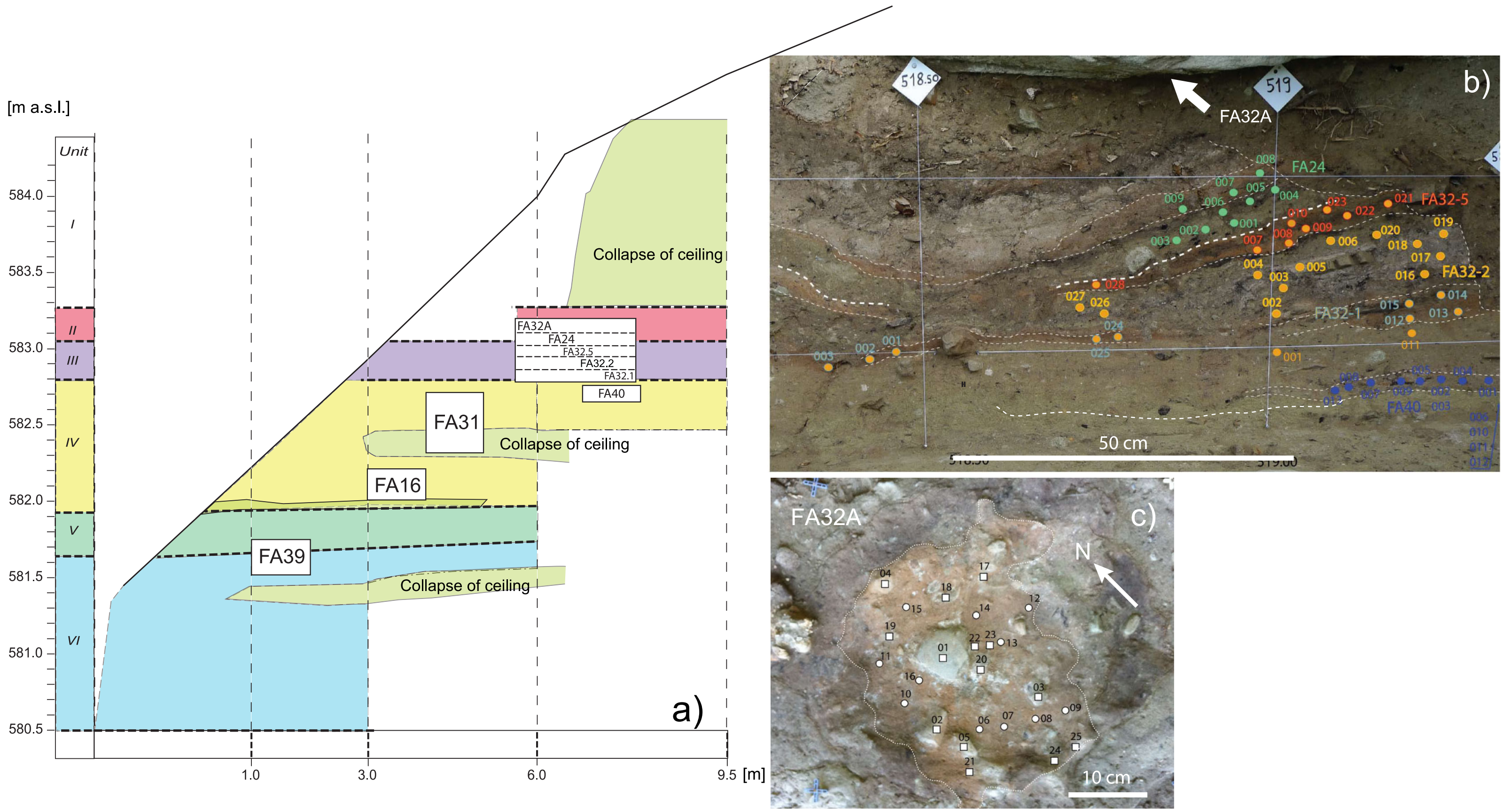

Figure 2. (a) Schematic picture of the excavated stratigraphy that shows the nine investigated fireplaces, which are marked with white boxes. (b) Stratigraphic succession from FA24 to FA40. Coloured dots represent the positions of the samples taken horizontally from a vertical cross section. (a) and (b)The NW–SE profile. (c) Example of sampling at fireplace FA32A as viewed from above. White squares show the positions of the vertically taken block samples, white circles show cylindrical samples taken with the hand corer. Numbers shown in (b) and (c) denote samples taken of each fireplace.

Table 1. Radiocarbon dates, calibrated ages and ages based on the model stratigraphy.

Name	Material	Fireplace	Unit	$Age_{\mathrm{uncal}} \pm \sigma$ (BP)	Age_{cal} (BC)	Age_{mod} (BC)
Ua-43129	Charcoal	FA32A[1]	II	6032 ± 33	4990–4890	4995–4840
Ua-43315	Bone	FA32A[1]	II	5995 ± 43	4950–4830	4995–4840
Ua-37285	Charcoal	FA24	II	6600 ± 45	5570–5490	5620–5480
–	–	FA32-5*	II	–	–	5660–5620
–	–	FA32-2*	II	–	–	5760–5660
–	–	FA32-1*	II	–	–	5810–5760
Ua-37283	Charcoal	FA06[2]	III	6715 ± 45	5670–5610	5840–5720
Ua-45037	Charcoal	FA06[2]	III	7025 ± 42	5990–5880	5840–5720
Ua-37284	Charcaol	FA19	III	7005 ± 50	5930–5830	5900–5740
Ua-43131	Charcoal	FA40	IV	6967 ± 45	5900–5780	5980–5810
–	–	FA31*	IV	–	–	6100–5885
Ua-23586	Charcoal	–	IV	7085 ± 60	6070–5800	6060–5890
Ua-33243	Charcoal	FA16	IV	7225 ± 60	6110–6020	6220–6010
Ua-41124	Charcoal	–	IV	7579 ± 46	6470–6410	6490–6260
Ua-45041	Charcoal	FA78	V	7696 ± 45	6590–6470	6600–6460
Ua-43130	Charcoal	FA39	VI	7744 ± 57	6640–6500	6680–6530
Vera-2904	Charcoal	FA15[3]	VI	7840 ± 35	6830–6560	6750–6610
Ua-41123	Charcoal	FA15[3]	VI	7894 ± 47	6830–6640	6750–6610

Notes: Age_{uncal} is the uncalibrated ^{14}C age. Age_{cal} gives the calibrated radiocarbon age within its 2σ boundary. Age_{mod} is the calibrated age further constrained by the model of the stratigraphy with its 2σ boundary. Superscript numbers in the column 'Fireplace' mark dates, which belong to the same layer and were combined in the age model (marked as 'Comb.' in Fig. 3). Fireplaces with a star have no radiocarbon dates, but their ages were estimated from the age model, as described in the text.

2.2 Sampling and sample preparation

A total of 130 samples were collected from nine fireplaces during five field campaigns. We obtained either cylindrical samples with a hand corer, which were pushed into plastic cubes with a volume of 3.9 cm^3 and an inner diametre of 1.6 cm, or block samples, which were covered with plaster on site and then consolidated and cut into cubes (2 cm edge length) in the laboratory. A magnetic and a sun compass were used to orient the samples.

2.3 Chronology

Radiocarbon ages were obtained from charcoal, seeds, charred wood and burned bones from Units II to VI, in order to study and refine the chronology of the periods of use and abandonment of the shelter (Table 1). They were dated at the Ion Beam Laboratory at ETH Zurich (Switzerland) and at the Angstrom Laboratory in Uppsala (Sweden). Three out of four dating attempts on bones were unsuccessful, but seeds and charred wood yielded precise results. To constrain the age sequence, the stratigraphic information was integrated within an age model using Oxcal v4.1.7 (Bronk Ramsey 2009) and the IntCal09 calibration curve (Reimer *et al.* 2009, Fig. 3, Table 1). We used 14 radiocarbon dates for age model; ages from the same layers were combined (FA32A, FA06 and FA15).

Sedimentation rates were estimated from the age model assuming a linear sedimentation rate for each unit and the thickness of the units. Unit II has the smallest sedimentation rate of 0.19 mm yr^{-1}, followed by larger rates for Unit III (2.00 mm yr^{-1}), Unit IV (1.38 mm yr^{-1}) and Unit V (2.50 mm yr^{-1}). The fastest rate was calculated for Unit VI with 8.46 mm yr^{-1}. The low sedimentation rate of Unit II may be explained by fewer occupations, and therefore also fewer deposits from the roof. Despite the large number of dated charcoal samples, four sampled hearths (FA31, FA32-1, FA32-2, FA32-5) have no associated absolute age. The ages of these hearths were estimated based on their position in the stratigraphy and the ages inferred from the age model (Table 1).

3 MEASUREMENTS AND METHODS

3.1 Rock magnetic measurements

A variety of rock magnetic experiments were carried out at the Laboratory for Natural Magnetism of the ETH Zurich (Switzerland) to identify the magnetic mineralogy, thermal stability and grain sizes of the studied samples. These include thermomagnetic curves, acquisition of an isothermal remanent magnetization (IRM) and thermal demagnetization of a cross-component IRM (Lowrie 1990), hysteresis curves (*cf.* Day *et al.* 1977; Dunlop 2002), and analysis of first-order reversal curves (FORC; Roberts *et al.* 2000). Viscosity tests were made to further assess the stability of the remanent magnetization, and the anisotropy of magnetic susceptibility (AMS) was determined to examine any possible compaction effect on the magnetic remanence. Thermomagnetic curves were measured using AGICO KLY-2 or MFK 1-FA susceptibility bridges with a CS-2 and CS-4 heating system, respectively, by heating up to 700°C and subsequently cooling back to room temperature. Heating and cooling rate was 11°C min^{-1}, and measurements were made either in air or argon atmosphere. IRM in a backfield was measured on a Princeton Measurement Corporation Micromag 3900 vibrating sample magnetometre (VSM) using a 3–10 mT sampling interval. Afterwards curves were smoothed with a 5- or 10-point running average. For the cross-component experiment, the IRM was imparted using an ASC scientific impulse magnetizer (Model IM-10-30). A 2000 mT field was applied along the sample z-axis, followed by a 460 mT field along the sample y-axis and finally a 200 mT field along the sample x-axis. An ASC scientific oven was used to thermally demagnetize samples; remanent magnetization was measured using a 2G Enterprise model 755R 3-axis DC-SQUID rock magnetometre. Hysteresis loops and first-order reversal curves were made on the VSM. FORC data was processed with the software of Harrison & Feinberg (2008). Viscosity tests were performed after three weeks of storage in zero field. The viscosity coefficient ν is calculated as

$$\nu = \frac{|\mathrm{NRM}_0 - \mathrm{NRM}_n|}{\mathrm{NRM}_0} \cdot 100 \quad (1)$$

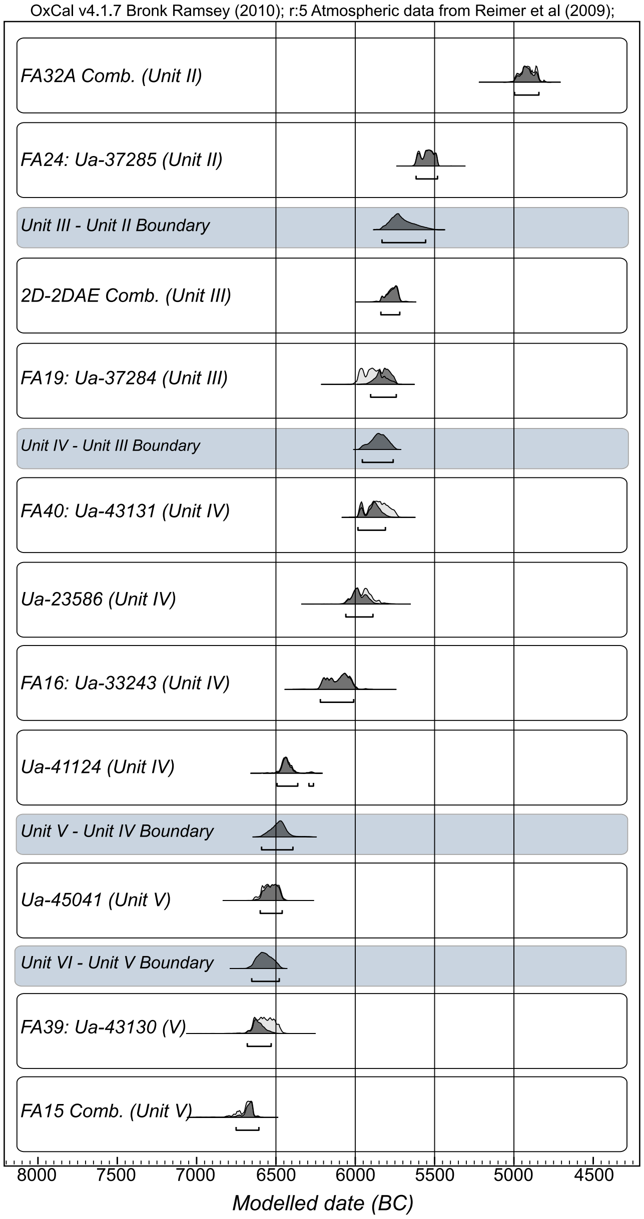

Figure 3. Radiocarbon ages and their stratigraphic position. Light grey probability distributions are the calibrated age ranges (Table 1: Age_{cal}), dark grey are the finally modelled distributions (Table 1: Age_{mod}). Each white box represents either one or several ages from one unit (marked as Comb). Unit boundaries are shown with respect to archaeological units. Age ranges of FA06 do not overlap, hence, no combined probability distribution for the calibrated ages can be calculated (light grey, 2D-2DAE).

where NRM_0 is the initial natural remanent magnetization (NRM) and NRM_n is the NRM after three weeks. We consider a viscosity coefficient smaller than 10 per cent as low. Bulk susceptibility (χ) was measured with an AGICO KLY-2 susceptibility bridge, using an applied field of 300 Am^{-1} and 920 Hz, on all samples. The Koenigsberger ratio Q (Koenigsberger 1938) was calculated using the formula

$$Q = \frac{\mathrm{NRM}}{H \cdot \chi} \tag{2}$$

chosing the field strength, $H = B/\mu_0$, for the Earth's magnetic field with $B = 50\,\mu\mathrm{T}$ and permeability of free space $\mu_0 = 4\pi \times 10^{-7}\,\mathrm{Hm}^{-1}$. AMS was measured with an AGICO KLY2 susceptibility bridge ($H_{\mathrm{app}} = 300\,\mathrm{A}m^{-1}$, 920 H$z$) and the principal axes of the anisotropy ellipsoid, $k_1 \geq k_2 \geq k_3$, are used to define the corrected anisotropy degree, P_j (Jelínek 1981) and the shape of the ellipsoid, T (Jelínek 1981), where

$$P_j = \exp\left[\left(2 \cdot \left((\eta_1 - \eta)^2 + (\eta_2 - \eta)^2 + (\eta_3 - \eta)^2\right)\right)^{-\frac{1}{2}}\right] \tag{3}$$

with

$$\eta_i = ln\, k_i \tag{4}$$

$$\eta = \frac{\eta_1 + \eta_2 + \eta_3}{3} \tag{5}$$

and the shape parameter

$$T = \frac{2\eta_2 - \eta_1 - \eta_3}{\eta_1 - \eta_3}. \tag{6}$$

Anisotropy data were processed with the Anisoft software (Agico).

3.2 Archaeomagnetic measurements

Samples were demagnetized using either progressive alternating field (AF) demagnetization or by stepwisely heating up to 580 °C (thermal demagnetization). Remanent magnetization was measured with the aforementioned DC-SQUID rock magnetometre, which is equipped with a 2-axis AF demagnetizer. Thermal magnetization experiments were carried out in an ASC Scientific oven, which has separate heating and cooling chambers. The remaining magnetic field in the cooling chamber is <3 nT. We applied principle component analysis (PCA) to isolate the characteristic component of the remanent magnetization (ChRM), using PmagPy-2.75 MagIC software (Tauxe *et al.* 2010).

In a first step, components of magnetization were accepted when at least four data points were used in the PCA, and the fitted line had a maximum angular deviation (MAD) $\leq 5°$ (Kirschvink 1980). Effects of possible post-burning disturbances in the fireplaces induced by animals or human activities may cause diverging directions within a sample, or even reversed inclination, when the magnetic grain has been completely disturbed from its original position. Samples with reversed inclinations were therefore systematically rejected. A sample may not entirely be affected by post-depositional disturbances. In order to objectively reduce spurious directions of single specimens we applied in a second step a hierarchical weighted average approach, which has already been used in Kapper *et al.* (2014). In the undisturbed case magnetizations of specimens from one fireplace are supposed to point in the same direction, regardless to which sample they belong. Hence, we apply the weighted outlier approach on specimen level. In this approach we first calculated the specimen average (Fisher mean) and assigned weights to each individual specimen, based on the distance from the Fisher mean and proportional to the 2σ range of the Fisher mean. Secondly, specimens with weights below 0.3 were rejected and considered outliers. Finally, we proceeded with the standard hierarchical approach, averaging the new set of specimens into sample averages and then calculating the averages for each fireplace. 22 per cent of the specimens had weights below 0.3, and were rejected. Weights of all specimens are on average 0.70 ± 0.05.

Table 2. Rock magnetic results of Arconciel samples.

Fireplace	B_c (mT)	B_{cr} (mT)	M_{rs}/M_s	B_{cr}/B_c	T_{ub} (°C)	χ ($x10^{-6}$)	NRM (mAm^{-1})
FA16	7.9 ± 1.2 (6)	24.4 ± 3.9	0.15 ± 0.02	3.11 ± 0.21	606 ± 37 (2)	3035 ± 135 (2)	168.2 ± 167.8 (10)
FA24	8.7 ± 3.1 (5)	27.0 ± 12.1	0.14 ± 0.01	3.07 ± 0.26	612 ± 37 (2)	2471 ± 1552 (9)	18.4 ± 15.8 (6)
FA31	8.5 ± 3.2 (4)	27.0 ± 9.0	0.11 ± 0.03	3.21 ± 0.32	586 ± 55 (2)	1405 ± 445 (21)	12.2 ± 11.8 (19)
FA32-1	7.8 ± 0.6 (6)	22.9 ± 2.1	0.14 ± 0.01	2.96 ± 0.05	592 ± 14 (2)	2330 ± 538 (9)	23.5 ± 11.8 (7)
FA32-2	–	–	–	–	584 ± 5 (4)	2448 ± 811 (11)	15.6 ± 8.5 (10)
FA32-5	8.3 ± 1.5 (3)	24.5 ± 3.6	0.14 ± 0.01	2.94 ± 0.15	588 ± 7 (3)	2097 ± 604 (8)	18.0 ± 7.8 (8)
FA32A	13.1 (1)	38.2	0.16	2.90	601 ± 23 (1)	1178 ± 262 (10)	14.0 ± 4.6 (10)
FA39	5.6 ± 0.9 (2)	13.6 ± 0.5	0.15 ± 0.02	2.43 ± 0.28	585 ± 1 (2)	2177 ± 1746 (16)	8.5 ± 2.1 (3)
FA40	7.3 ± 1.4 (4)	23.0 ± 3.2	0.14 ± 0.01	3.16 ± 0.18	598 ± 4 (3)	4143 ± 1430 (11)	30.8 ± 28.8 (15)

Notes: B_c, coercivity; B_{cr}, coercivity of remanence; M_{rs}, saturation remanence; M_s, saturation magnetization; T_{ub}, unblocking temperature; χ, bulk magnetic susceptibility; NRM, natural remanent magnetization. Numbers in brackets are the amount of measured samples. Numbers in the first column apply as well to the second to fourth column.

4 RESULTS

4.1 Rock magnetic results

Rock magnetic results for each fireplace are summarized in Table 2. A total of 27 thermomagnetic determinations were made, of which 16 were measured in air and 11 in argon environment. Measurements in argon environment do not show more reversible curves than those measured in air, although Curie temperatures (T_c) were always lower than 595°C in samples measured in argon. From these data we calculate the T_c based on the differential method by Tauxe (1998) and obtain an average T_c of 590 °C. Several samples showed that a new ferromagnetic phase is created starting around 400 °C, which is stable upon cooling (Fig. 4a). In all fireplaces, except in FA39, we found at least one thermomagnetic curve with a T_c between 600 and 640 °C (Fig. 4b).

IRM acquisition in a backfield reveals coercivities of remanence, B_{cr}, between 13.6 mT for FA39 and 48.1 mT for FA24, with an average of 25.1 ± 6.8 mT for all nine fireplaces (Fig. 5, Table 2). The IRM of most samples is saturated at 300 mT. The cross-component IRM shows that all samples are dominated by the soft component ($\leq$ 0.2 T), which has a maximum unblocking temperature of around 580 °C (Fig. 6a). In nearly all layers we found that the soft component also showed another unblocking around 620 °C, which might originate from another low coercivity mineral.

The majority of the 44 measured hysteresis loops have a narrow shape that is closed by 300 mT (Fig. 7a); three samples from FA40 and FA16 show slightly wasp-waisted loops. Coercivities, B_c, are 8.4 ± 2.1 mT on average. Loops from fireplaces FA24, FA32-5, FA31 and FA32A have slightly larger B_c (12.5 mT on average). Fig. 7(b) shows that all specimens fall into the pseudo-single domain (PSD) field of the Day–Dunlop plot, with average M_r/M_s-ratios of 0.14 ± 0.01 and B_{cr}/B_c-ratios of 2.97 ± 0.24. FORC analysis shows that the samples can be divided into three types of behaviour (Fig. 8). In the first case samples show a broad coercivity distribution between 0 and 60 mT with a single peak in the coercivity around 8 mT (Fig. 8a). The interaction field, B_u, is about ±20 mT. The second behaviour shows two distinct coercivity peaks (Fig. 8b). The first is centred around 1–2 mT and the second peak around 8 mT. The interaction field in this case is narrower and lies between ±10 mT. The third behaviour lies between these first two cases with a peak near 0 mT and a second broader plateau centred around 8 mT (Fig. 8c). Most samples show this third behaviour. The lower coercivity peak suggests the presence of superparamagnetic particle size, which is also expressed by the tail in the FORC distribution at 0 mT for negative B_u (Pike *et al.* 2001).

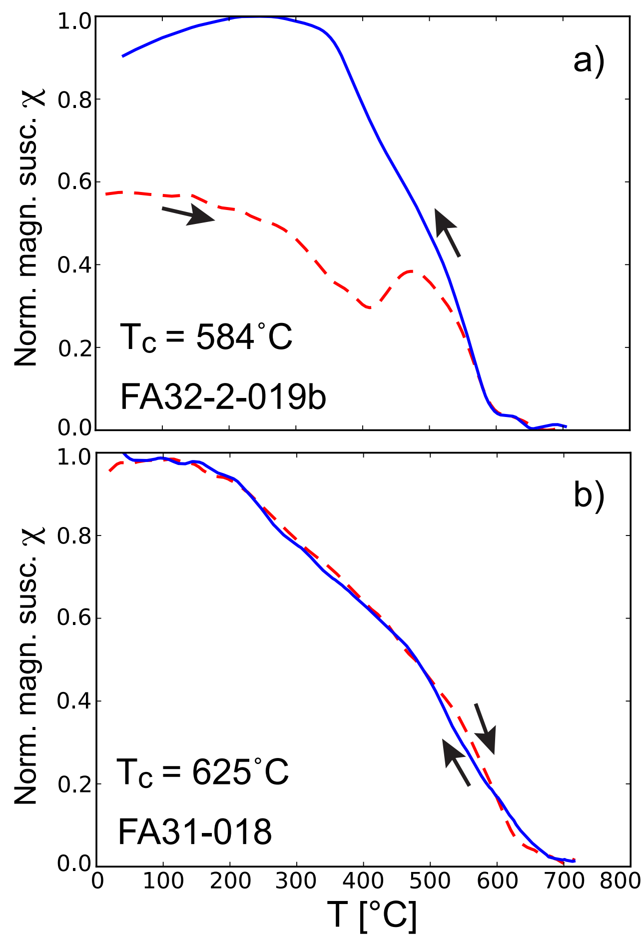

Figure 4. Thermomagnetic curves for representative sample. Magnetic susceptibility is normalized to the maximum value; the red dashed line shows the heating curve and the blue continuous the cooling curve.

AMS was used to investigate if the samples show any significant compaction, which may deflect the remanent magnetization. The minimum magnetic susceptibility, k_3, clusters to the SW with an average inclination of 40° away from the centre of the stereoplot for all fireplaces (Fig. 9a). The medium, k_2, and maximum, k_1, susceptibilities are distributed in a girdle in a plane normal to the k_3 axes. Fig. 9(b) shows the corrected anisotropy degree P_j versus bulk susceptibilities χ_m. Average P_j is (2.2 ± 0.1) per cent excluding the four specimens with high P_j (Figs 9b and c). Fig. 9(c) shows shape

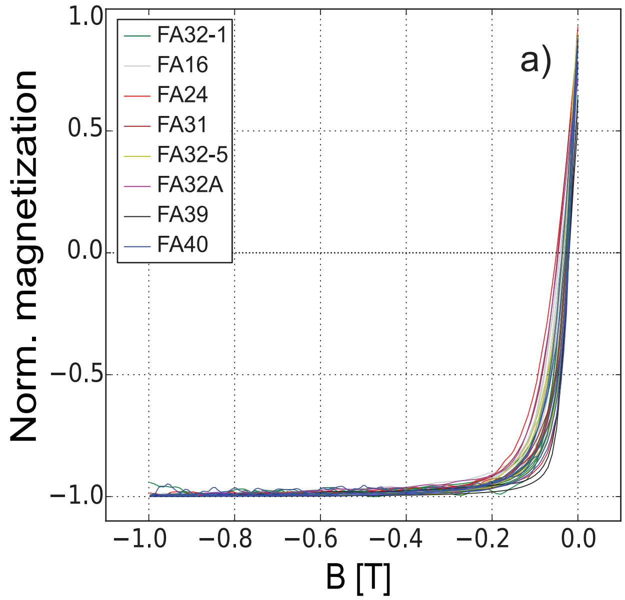

Figure 5. Backfield IRM acquisition curves for representative samples. IRM is first smoothed and then normalized by the absolute value of its minimum IRM.

parameter T versus anisotropy degree P_j. Most samples have an oblate shape with $T > 0$, up to rotational oblate shape with $T = 1$. Average bulk susceptibilities are largest for FA40 with $(4143 \pm 11430) \times 10^{-6}$ SI (Table 2).

Fig. 10(a) shows NRM versus bulk magnetic susceptibility with lines of constant Q. Specimens have Q values between 0.1 and 1 for the majority of samples. FA31 shows the highest variability within a single fireplace, and samples from FA32A and FA39 show highest Q values on average. Viscosity tests on seven selected specimens show that the amount of viscosity is related to the intensity of NRM, with high viscosity coefficient for weaker NRM (Fig. 10b). One specimen from FA24 shows an extremely large viscosity of around 45 per cent. Further viscosity test are needed to investigate if more samples of FA24 have similar high-viscosity coefficients or if this specimen is an outlier.

4.2 Archaeomagnetic directions

A total of 140 specimens were demagnetized with AF or thermal demagnetization (Table 3), and 91 fulfilled the quality criteria (cf. Section 3.2). Most samples possess either a single component of magnetization, the characteristic remanent magnetization (ChRM) or two components: the ChRM and a viscous component (Fig. 11). For specimens, which were demagnetized in an AF, the ChRM is generally isolated in the linear fraction between 4 and 46 mT, and a viscous component is at the low coercivity portion of the vector diagram. An exception is specimens from FA16, of which the ChRM ranges from 18 to 86 mT on average with a larger viscous component (Fig. 11a). Most of the specimens of FA16 are not demagnetized at 160 mT, which could be indicative for a high-coercivity magnetic mineral. Largest NRM values were observed in FA16, FA40 and FA32-1 (Table 2). For FA39 90 per cent of magnetization was demagnetized at low field strengths of 28 mT on average, followed by FA40 by 34 mT, whereas FA16 and FA32A lost 90 per cent of their magnetization at 85 mT and 100 mT, respectively. Vector fits to the demagnetization are well-defined with MAD $\leq 3^{\circ}$ for most specimens.

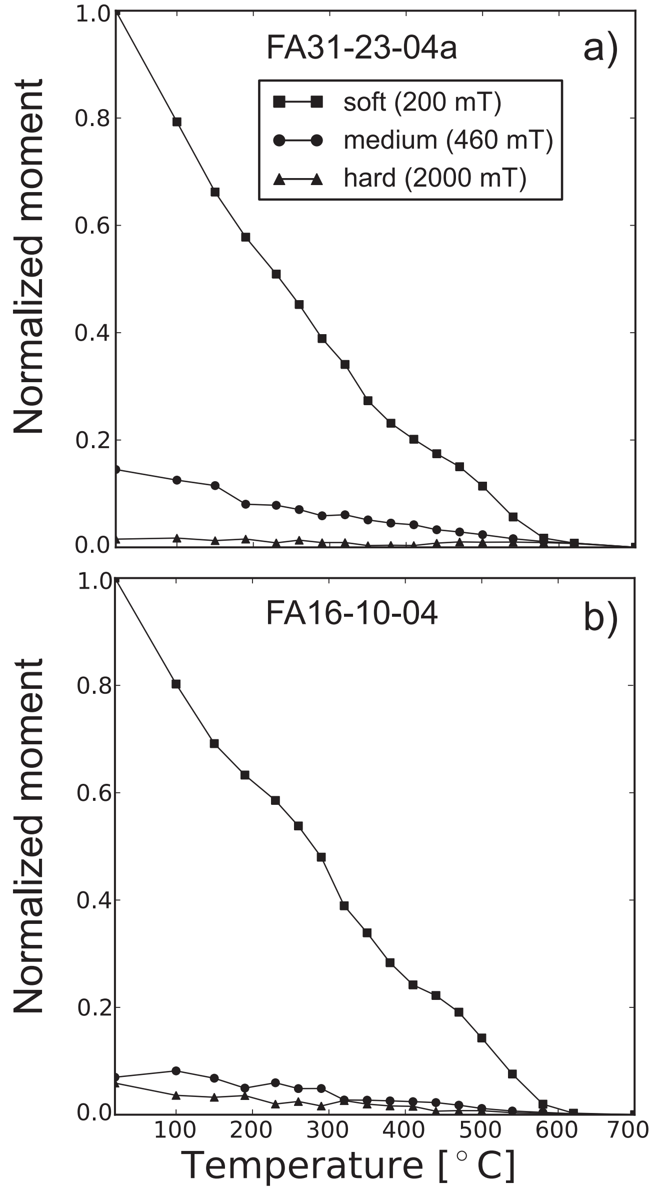

Figure 6. Progressive thermal demagnetization of a cross-component IRM as a function of temperature. IRM intensity has been normalized by the maximum value of the soft component.

Fifteen specimens from FA16 were thermally demagnetized, of which twelve were accepted. The PCA comprises eleven temperature steps on average. Vector diagrams show either a ChRM or a ChRM and a small viscous component. Directions are well-defined with a MAD of $(2.3 \pm 0.8)^{\circ}$. All specimens have lost at least 80 per cent of their magnetization at 580 °C. After removing outliers with the weighted average approach best-grouped fireplace means are given in Table 3.

5 DISCUSSION

5.1 Types of magnetic minerals and stability of magnetization

Rock magnetic measurements show that all fireplaces have similar magnetic properties. The main magnetic carrier is magnetite, which was identified by maximum unblocking temperatures close

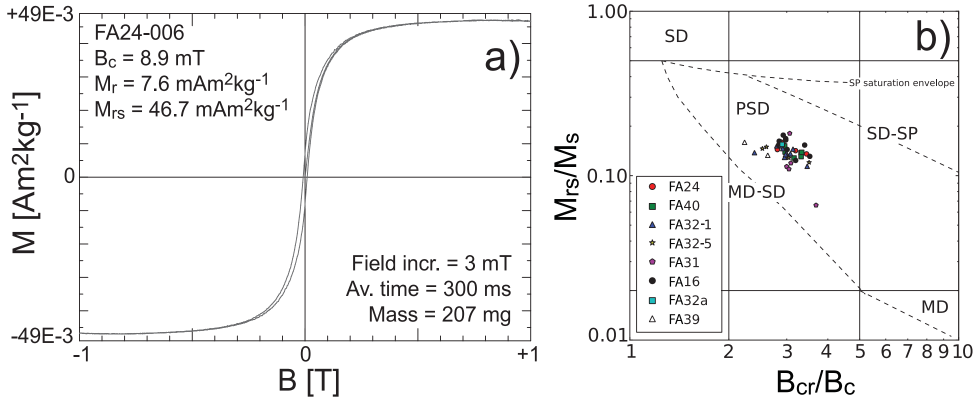

Figure 7. (a) Example of a typical hysteresis loop after dia- and paramagnetic slope correction (70 per cent of the maximum signal). (b) Day–Dunlop plot showing magnetization and coercivity ratios for a typical selection of samples. The MD-SD and SD-SP mixing lines (dashed) refer to the caluclations of Dunlop (2002).

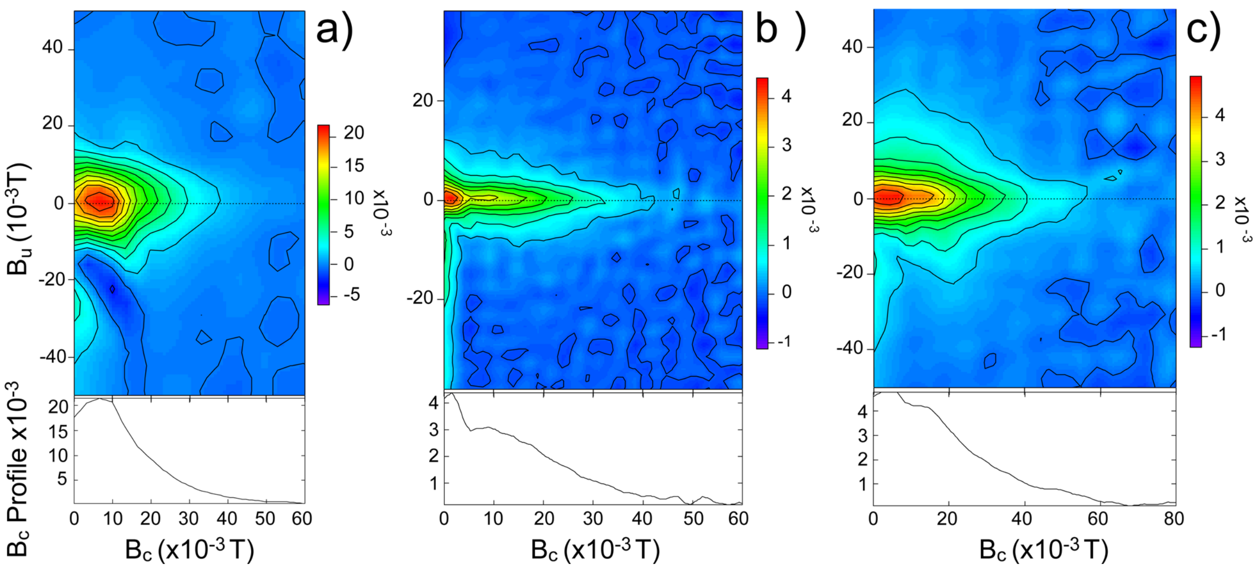

Figure 8. Examples for FORC diagrams (above) and their corresponding coercivity profiles (below) for (a) FA39-2, (b) FA16-008 and (c) FA24-006.

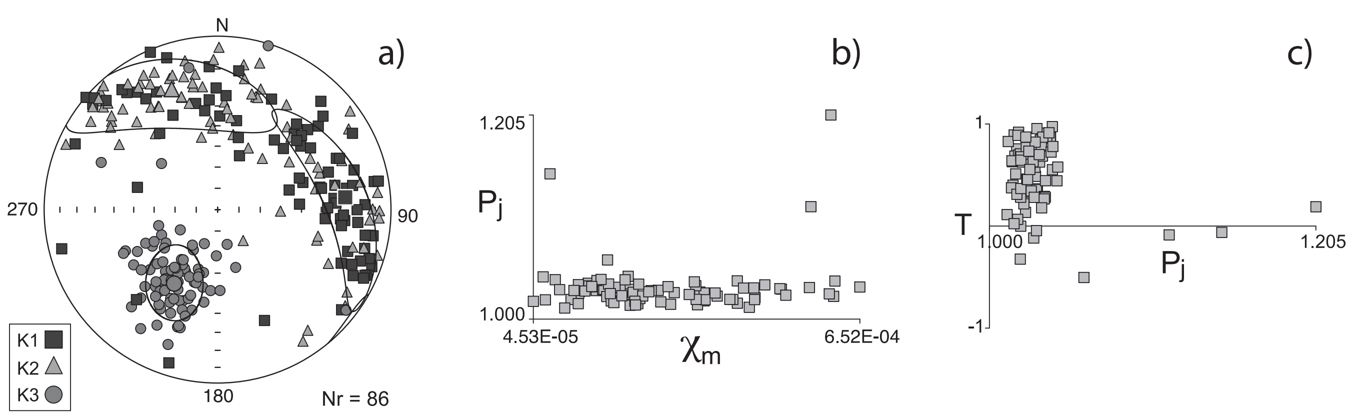

Figure 9. (a) Anisotropy of susceptibility for all specimens. Squares represent maximum k_1, triangles intermediate k_2 and circles minimum k_3 susceptibilities. Larger symbols are averages for the principal axes, and ellipses are 95 per cent confidence intervals. Data are plotted on an equal-area, lower hemisphere projection in geographic coordinates. (b) Anisotropy degree P_j versus average bulk susceptibility χ_m. (c) Shape parameter T versus P_j.

to T_c = 585 °C in thermomagnetic curves (Fig. 4a) and the cross-component experiment (Fig. 6a). Some samples have a low coercivity phase that is completely unblocked at 620 °C in the cross-component experiment, which indicates a phase between magnetite and maghemite (Fig. 6b, soft component). Similar high unblocking temperatures in low coercivity minerals have been observed in other archaeomagnetic studies (e.g. Chauvin *et al.* 2000; Carrancho *et al.* 2009). A few samples from FA31, FA16, FA32A and FA32-1

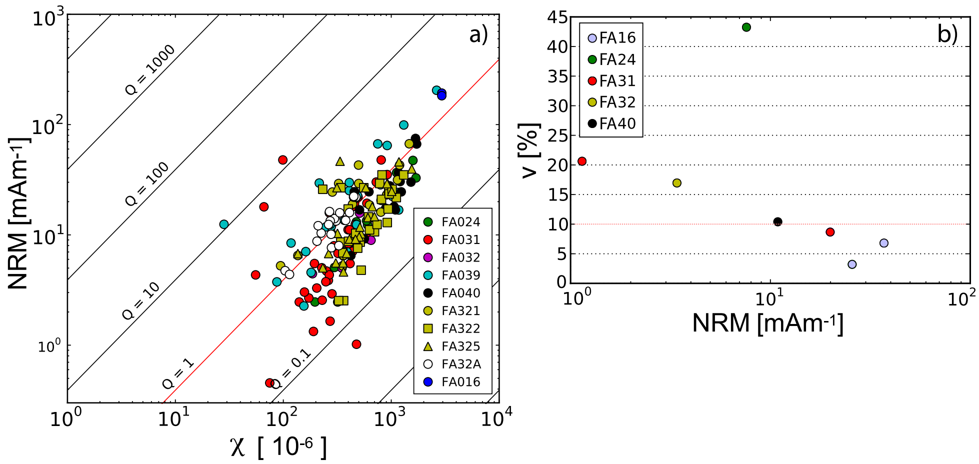

Figure 10. (a) Natural remanent magnetization (NRM) versus bulk magnetic susceptibility (χ) showing lines of constant Koenigsberger ratio (Q). (b) Viscosity coefficient versus NRM for seven specimens.

Table 3. Directional results of ARC fireplaces.

Level/Fireplace	N_s/N_{sac}	N_{sp}/N_{spac}	D (°)	I (°)	α_{95} (°)	k ()	R ()	Age (BC)
FA39	13/9	15/10	359.2	59.8	2.8	329.3	9.0	6635
FA16	10/9	28/20	11.9	56.1	5.8	79.0	8.9	6065
FA31	14/8	17/9	18.7	56.1	7.9	50.1	7.9	5990
FA40	9/7	14/8	29.4	61.9	9.1	44.9	6.9	5885
FA32-1	5/4	8/6	10.6	73.1	9.8	88.8	4.0	5780
FA32-2	7/5	13/8	16.4	70.0	9.6	64.7	4.9	5710
FA32-5	8/6	13/8	22.6	61.8	6.9	96.2	5.9	5640
FA24	6/5	9/6	19.6	64.6	2.9	703.5	5.0	5535
FA32A	10/9	20/14	342.9	58.6	4.8	113.8	8.9	4930

Notes: FA represents individual ARC fireplaces. N_s is the total number of samples, N_{sac} the number of accepted samples. N_{sp} is the total number of specimens, N_{spac} the number of accepted specimens. Declination (D) and inclination (I) of Fisher mean of each fireplace, α_{95} is the confidence interval around the Fisher mean, k the precision parameter. R is the length of the vector sum, and Age the modelled age, which is the age at maximum probability of the dark grey age distributions shown in Fig. 3 for the ARC samples. Please refer to the corresponding age ranges in Table 1 in the last column.

also possess a high-coercivity component that does not saturate by 1 T, which is most likely hematite. Most samples fall into the PSD area on a Day plot (Fig. 7b), with some superparamagnetic contribution, as seen in FORC analysis (Fig. 8b and c). The AMS ellipsoid displays the compaction and the original tilt of the layers, which belong to concave fireplaces. Nevertheless, archaeomagnetic directions do not show a tilt or flattening. This discrepancy may indicate that the AMS ellipsoid is carried by the paramagnetic minerals. Furthermore, the average P_j is very low with (2.2 ± 0.1) per cent excluding the outlying specimens, and therefore considered too insignificant to deflect the remanent direction (Fig. 9b and c). All investigated fireplaces yielded successful directions with low scatter in the stereoplots and $\alpha_{95} \leq 10°$, similar to results from other burned sediments (Fig. 12; e.g. Carrancho *et al.* 2013). Fireplaces from ARC exhibit a stable magnetization in general, because vector diagrams have a single component of magnetization (Fig. 11). Samples with the most stable magnetizations are from FA32A and FA39, which have the largest Koenigsberger ratios and the most clustered (lowest α_{95} and largest k values) sample directions in the stereoplots (Fig. 12). Fireplaces FA16 and FA40 have lowest viscosity coefficients, which indicates little alteration of magnetization (Fig. 10b). Fireplace FA24, which shows the largest viscosity coefficient, has very clustered directions with a k of 703.5 (Fig. 12, Table 3).

5.2 Smoothing spline fit

To calculate continuous secular variation curves for declination and inclination, we fit a curve to the data points using the technique of penalized least square spline (PLSS; e.g. Constable & Parker 1988), The aim of the PLSS method is to find the smoothest twice differentiable function fitting the data points. Further, an L1 norm, the least-absolute deviation, of the residuals is used instead of the L2 norm. The L1, which was also used by Panovska *et al.* (2012) has been shown to reduce the influence of spurious data points by giving less weight to outliers than the L2 norm (Walker & Jackson 2000). The L2 exhibits less smooth variations, sometimes even unrealistic and fast changing behaviour. Furthermore, the L1 norm better fits unevenly distributed data, which is the case here. The basis functions for the fit are cubic splines, which are defined on a regular set of knot points with a fixed 50 yr spacing. A smoothing parameter, which controls the relation between the smoothness and the goodness of the fit to the data, is objectively chosen using the method of cross validation (CV, Green & Silverman 1994). The minimum of CV gives the smoothing parameter for the spline fit.

The smoothing spline fit technique was applied to the new ARC data from this study (Table 3) together with other archaeomagnetic data included in a circular area of 700 km radius around ARC

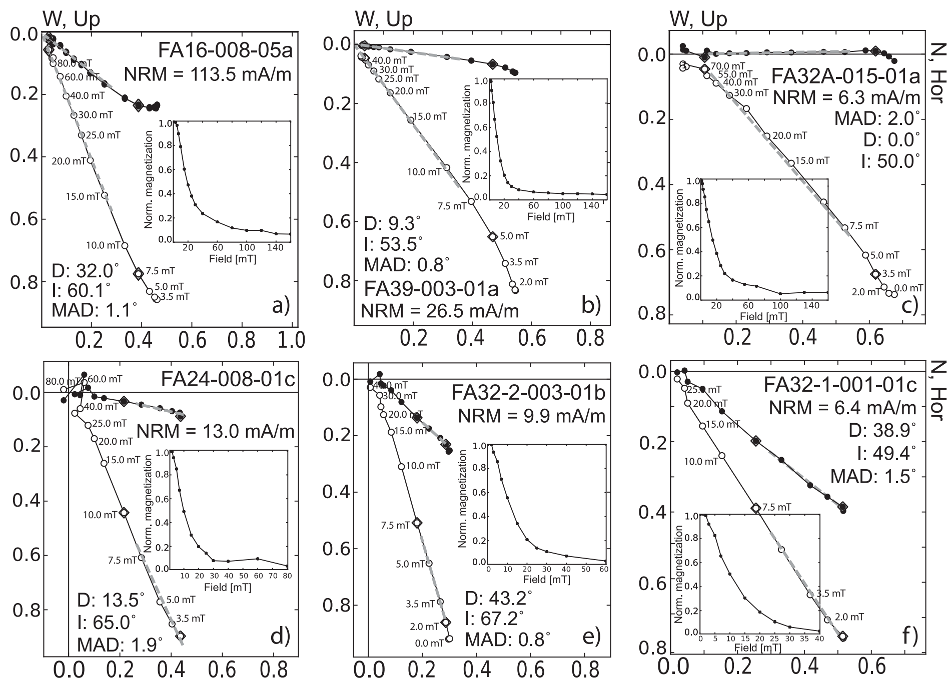

Figure 11. Vector diagrams (Zijderveld 1967) and corresponding normalized demagnetization diagrams (insets) for selected samples with horizontal (vertical) components shown with black (white) dots. Dashed lines with diamonds illustrate demagnetization steps used for PCA. D, declination; I, inclination; MAD, maximum angular deviation. The x-axis represents North and the horizontal plane and y-axis West and upward directions, respectively.

(Fig. 13). This area has been chosen to reduce the relocation error (Casas & Incoronato 2007), while all selected data are characterized by $\alpha_{95} \leq 10°$ and an age error < 150 yr. With these criteria we obtained 356 data points from France, England, Netherlands, Austria, Italy, Germany, Switzerland and Belgium from the Geomagia50v.2 database (Donadini *et al.* 2006; Korhonen *et al.* 2008, Fig. 13) and six data points from northern Italy (Kapper *et al.* 2014). For time periods with little or no data (4500–1000 BC), the spline fit can not be interpreted. The limited amount of data in these time periods leads to a limited resolution of the spline fit. The spline fits are used for comparisons with other archaeomagnetic data, lake sediment records and models.

5.3 Comparison with other data sets and models

Figs 14(a) and (b) show inclinations and declinations of ARC, which were relocated to the location of ARC (7.11°E and 46.76°N) using the conversion via pole method (Noel & Batt 1990), and cover the period between 7000 and 4900 BC. Casas & Incoronato (2007) show that relocation within Europe leads to relocation errors in declination and inclination of 0.25° per 100 km. However, this error is irrelevant when only the position of peaks is investigated, and not the absolute directional value. The data are presented together with other archaeomagnetic data, the archaeomagnetic spline fit, the Balkan curve of Tema & Kondopoulou (2011), and the European palaeosecular variation curve (PSVC; Carrancho *et al.* 2013). Another data point from a recent study, which is at present not in the Geomagia50 v.2 database, from Hervé *et al.* (2013) at 3730 BC is also shown. The archaeomagnetic spline fit has a maximum in inclination of 65° at around 5750 BC, followed by a decrease to 55° at 4700 BC. Further inclination maxima are observed at around 3300 BC, 500 BC, 750 AD and 1600 AD. The archaeomagnetic spline fit of declination shows an eastward trend between 6800 and 5900 BC, where a maximum declination value of 15° is observed. After this time, the trend changes to −17° in the west until 4200 BC. Compared with the Balkan curve and the European PSVC the spline fit shows similar trends over the entire time interval, although the period between 4500 and 1000 BC is constrained by only six data points and therefore, can not be considered reliable. Further, the peak in declination at around 5900 BC may occur about 700 yr earlier than the peak in the Balkan curve and approximately 1000 yr earlier than the peak in the European PSVC, although the peaks for inclination coincide. Hervé *et al.* (2013) noted similar time lags of 50 and 100 yr for the maxima in declination and inclination curves for Western Europe at Paris and Eastern Europe at Thessaloniki in the time period around 900 BC and 300 BC. This feature indicates a westward drift of secular variation from west to east, and is interpreted as westward drift of the fluid core. It may also be similar for the earlier time lag between the Balkan curve and the archaeomagnetic spline fit. Considering the distance between Thessaloniki, where the Balkan curve is centred, and Arconciel of about 1500 km, the lag in declination appears to move about 0.02 degrees yr^{-1} eastward starting at 5900 BC. The peak in declination might be a local event, which appears 700 yr later in the Balkan area. The European PSVC is mainly based on data from eastern Europe (Carrancho *et al.* 2013), and may therefore show more similarities in declination around 5900 BC to the Balkan curve, than to the archaeomagnetic spline fit.

Figs 15(a) and (b) show the spline fit of the archaeomagnetic data together with a spline fit from lake sediments taken from a single core at Lake Baldegg (Switzerland, 47.2°N, 8.3°E, BAL, Kind 2012), which is located in 140 km distance from the ARC shelter (Fig. 1). It is also compared to the stacked record from Fennoscandian lake sediments (FENN, Snowball *et al.* 2007), and to the detransformed UK lake sediments curve (UK, Turner & Thompson 1981, 1982; Vigliotti 2006). The BAL spline fit was produced with the same method as the archaeomagnetic spline fit. Declinations and inclination of the Fennostack record are relative. The detransformed

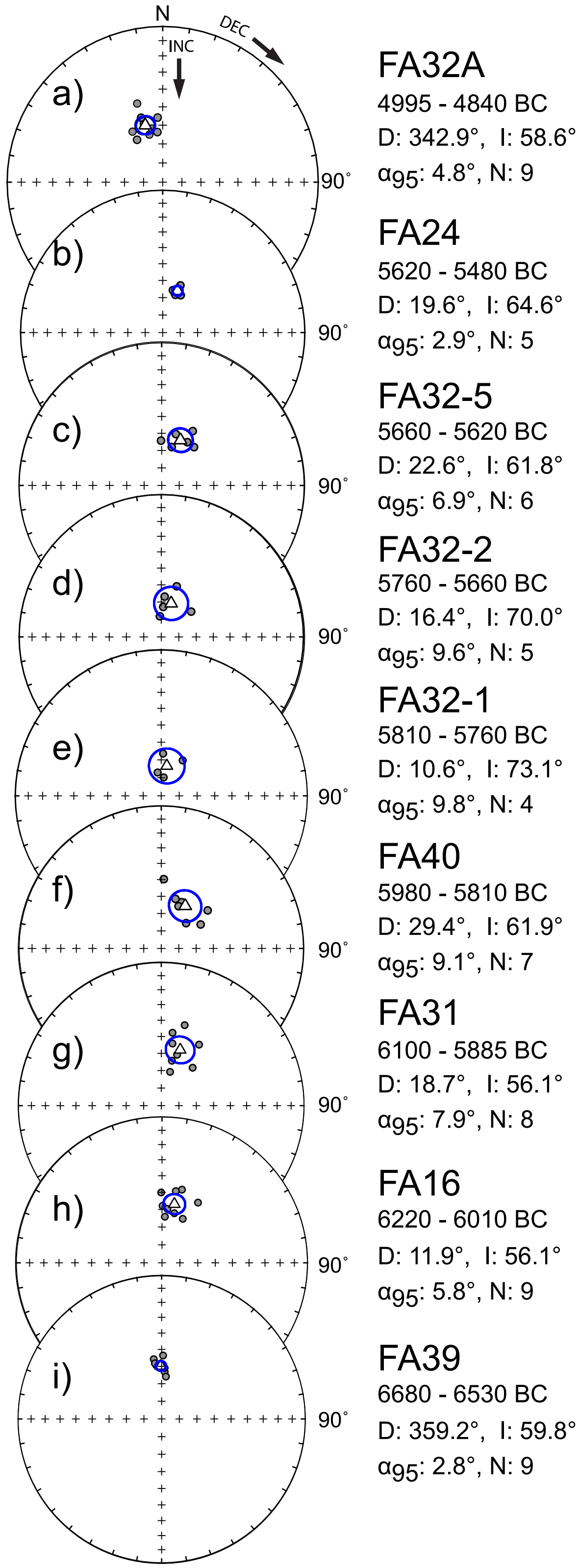

Figure 12. Stereoplots showing sample averages (black circles), fireplace Fisher means (white triangles) and α_{95}–confidence ellipses. N is the number of samples.

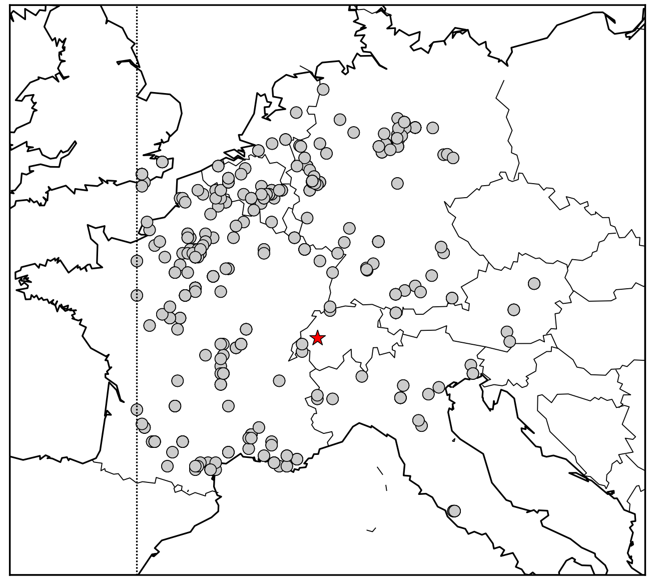

Figure 13. Locations of archaeomagnetic directional data, which were used for the archaeomagnetic spline fit (dots), from a circular area with a radius of 700 km around Arconciel (star). Data are from a time period between between 7000 BC and 1990 AD, and are taken from the Geomagia50v.2 database (Donadini *et al.* 2006; Korhonen *et al.* 2008) and from a site in northern Italy close to Trento (Kapper *et al.* 2014). The dashed line denotes zero longitude.

UK curve is absolute and relocated to London. To avoid relocation errors, especially for the UK and FENN curves, directions of UK and FENN were scaled by subtracting the median of the records and adding the median of the archaeomagnetic data used for the archaeomagnetic spline fit. The BAL spline fit was scaled with the same method to be consistent with the other curves. All three lake sediment curves show similar features as the archaeomagnetic spline fit, for example between 2250 BC and 2000 AD in inclination (Fig. 15a) and between 3500 BC and 1500 AD in declination (Fig. 15b). A similar lag in declination as the one observed in Fig. 14(b) for the Balkan curve appears in this comparison as well; in this case, the FENN record shows the youngest peak at 4700 BC, followed by the peak in UK curve at 5250 BC. On the contrary, the BAL fit, located close to ARC, shows largest values of declination around 5900 BC. The discrepancy in peaks both geographically and temporarily suggests that the records of individual regions contain local features. Also in inclination a time lag between the lake sediment curves and the archaeomagnetic spline fit is observed, with maxima in the FENN record at 6000 BC and in the UK curve at 6400 BC. In the same time period the BAL fit shows two maxima in inclination, one at 6000 BC and another one at 5600 BC, which coincides with a peak of the archaeomagnetic splin fit.

The comparison of the archaeomagnetic spline fit with two spherical harmonics models, the CALS10k.1b (Korte *et al.* 2011) and the SCHA.DIF.3k/8k (Pavón-Carrasco *et al.* 2009, 2010) is shown in Fig. 16(a) and (b). The CALS10k.1b shows a rather smooth behaviour over the entire Holocene interval because of the scatter in lake sediment directions that are used in the model (Korte *et al.* 2011). To overcome this problem, Pavón-Carrasco *et al.* (2010) selected lake sediment data based on their agreement with available archaeomagnetic data in the vicinity of the lake to produce the SCHA.DIF.8k, or only considered archaeomagnetic and instrumental data for the SCHA.DIF.3k model (Pavón-Carrasco *et al.* 2009). In this respect, the archaeomagnetic spline fit agrees well

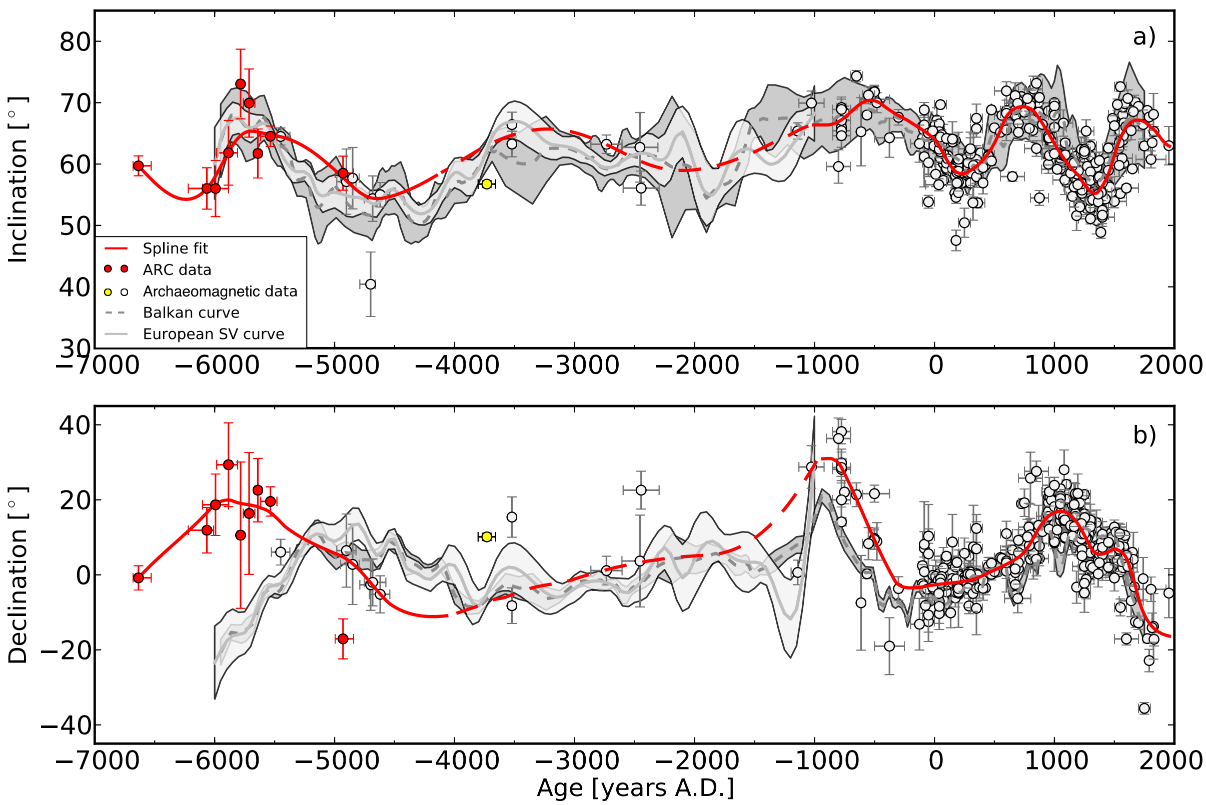

Figure 14. Spline fit of (a) inclination and (b) declination of the ARC data (red line and dots, respectively) and archaeomagnetic data from an area of 700 km around ARC (white dots). The dashed part in the spline fits denote the time period with little data. Further shown are the Balkan curve (dashed grey line) and its standard deviation, the European PSVC (continuous grey line) and its standard deviation, and archaeomagnetic data from a recent study (yellow dot, Hervé *et al.* 2013). All data are relocated to ARC (7.11°E and 46.76°N) using the conversion via pole method (Noel & Batt 1990).

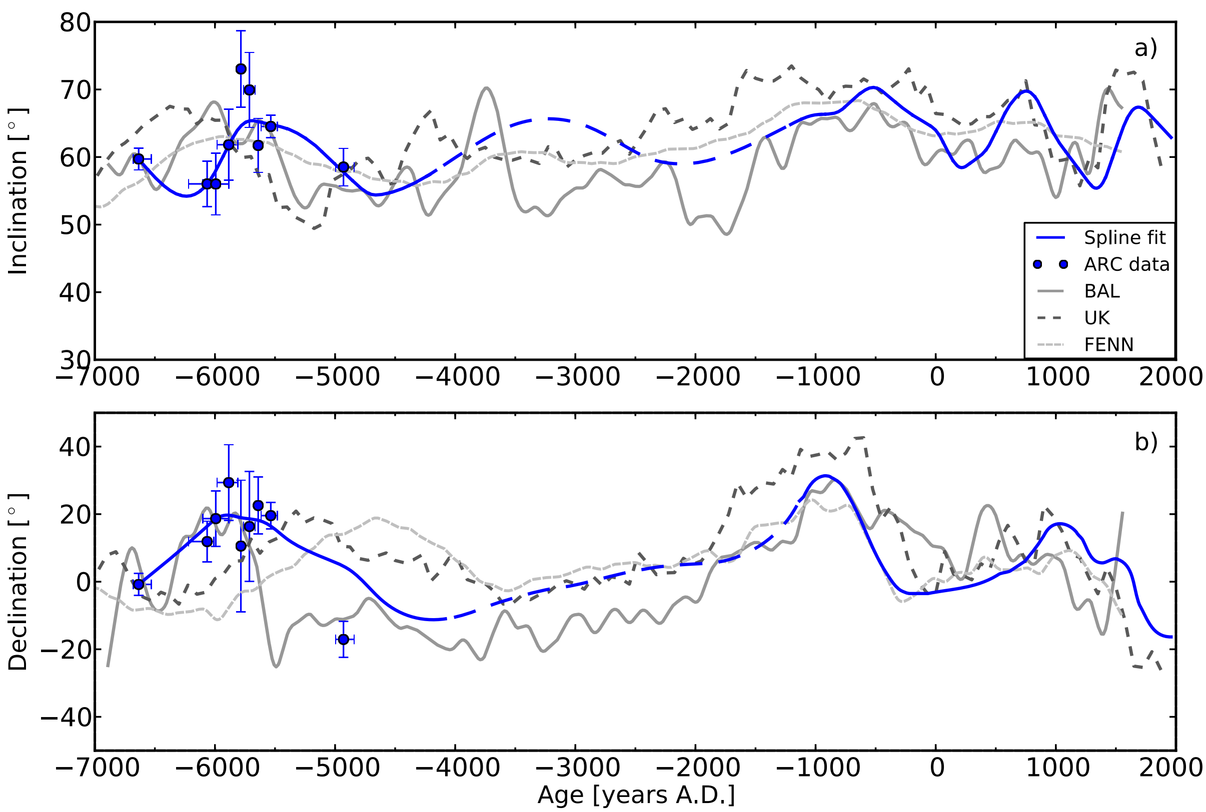

Figure 15. Spline fit of (a) inclination and (b) declination of the archaeomagnetic data and ARC data (blue line and dots) compared to spline fits of sediment data from Lake Baldegg (BAL), the UK lake curve (UK) and the Fennostack record (FENN).

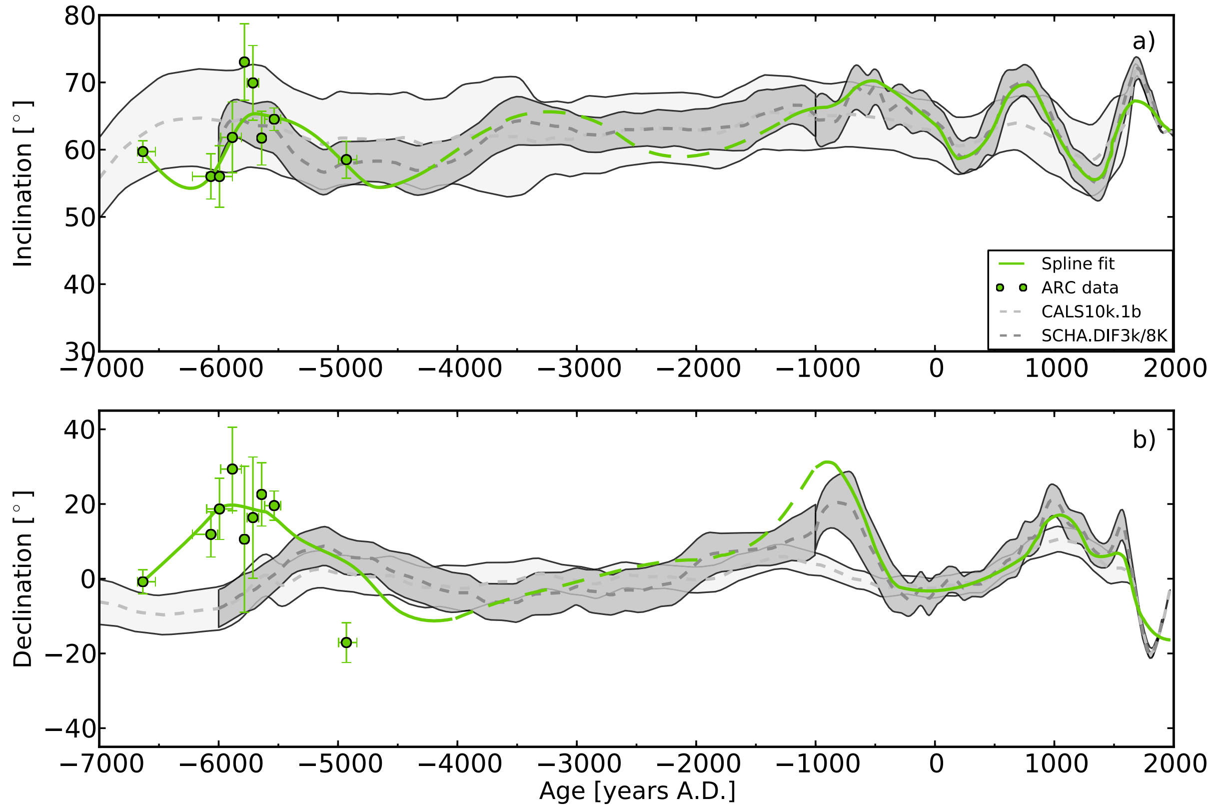

Figure 16. Spline fit of (a) inclination and (b) declination of the archaeomagnetic data and ARC data (green line and dots) compared to the CALS10k.1b model (light grey) and the SCHA.DIF.3k/8k (dark grey).

with the SCHA.DIF.3k and 8k. Again, the main difference appears to be the declination peak occurring at 5900 BC at ARC, which lags by about 700 yr in the regional spherical cap harmonic model. It must be noted, however, that most of the archaeomagnetic data used in the SCHA.DIF.8k is from Eastern Europe, for example Bulgaria and Ukraine; and lake sediment data, which makes the largest contribution to the SCHA.DIF.8k, is mainly from Scandinavia, UK and Italy. These discrepancies illustrate the importance of having a broad geographic distribution of data used in constructing field models, so that local features are not considered to represent global field behaviour.

6 CONCLUSIONS

This study illustrates the potential of fireplaces to record geomagnetic field variations. The directional results presented here show larger scatter than other archaeological materials such as ceramics, but are comparable to other studies on burned sediments. Directional data from this study can be combined with data from other archaeological studies within a 700 km circumference around Arconciel in order to construct a smoothed spline fit to describe secular variation for Central Europe. Similar behaviour is found between the temporal change in declination and inclination with the SCHA.DIF.3k/8k models. A good correlation is found between declination and inclination, obtained in this study and data from Lake Baldegg, which is located close by Arconciel. The declination peak that occurs at 5900 BC at Arconciel and Lake Baldegg occurs about 700–1000 yr earlier compared to Eastern and Northern European regions. These observations suggest that a local geomagnetic feature occurs in Central Europe in this time period, which might move to other European regions. New mid-Holocene archaeomagnetic data from nearby sites would be beneficial to verify the trend observed in this study, whereas data from distant sites may help in defining the extent of such feature.

ACKNOWLEDGEMENTS

This work was supported by ETH Research Grant ETH-12 10-2. We kindly acknowledge Jessica Kind for providing data from lake Baldegg. Furthermore, we thank L. Vigliotti for providing the new recalibrated UK lake sediment curve. Fabio Donadini gratefully acknowledges the support of a Swiss National Science Foundation grant (200021 130147). We highly appreciate the comments from the reviewers, Simo Spassov and Evdokia Tema.

REFERENCES

Bleil, U. & von Dobeneck, T., 1999. Geomagnetic events and relative paleointensity records – clues to high–resolution paleomagnetic chronostratigraphies of Late Quaternary marine sediments?, *Use of Proxies in Paleoceanography: Examples from the South Atlantic,* pp. 635–654, Springer.

Bronk Ramsey, C., 2009. Bayesian analysis of radiocarbon dates, *Radiocarbon,* **51**(1), 337–360.

Canti, M. & Lindford, N., 2000. The effects of fire on archaeological soils and sediments: temperature and colour relationships, *Proceedings of the Prehistoric Society,* **66,** 385–395.

Carrancho, A. & Villalaín, J., 2011. Different mechanisms of magnetisation recorded in experimental fires: archaeomagnetic implications, *Earth planet. Sci. Lett.,* **312,** 176–187.

Carrancho, A., Villalaín, J., Angelucci, D., Dekkers, M., Vallverdú, J. & Vergès, J., 2009. Rock-magnetic analyses as a tool to investigate archaeological fired sediments: a case study of Mirador cave (Sierra de Atapuerca, Spain), *Geophys. J. Int.,* **179,** 79–96.

Carrancho, A. *et al.*, 2013. First directional European palaeosecular variation curve for the Neolithic based on archaeomagnetic data, *Earth planet. Sci. Lett.,* **380,** 124–137.

Casas, L. & Incoronato, A., 2007. Distribution analysis of errors due to relocation of geomagnetic data using the Conversion via Pole (CVP) method: implications on archaeomagnetic data, *Geophys. J. Int.,* **169**(2), 448–454.

Chauvin, A., Garciao, Y., Lanos, P. & Laubenheimer, F., 2000. Paleointensity of the geomagnetc field recovered on archaeomagnetic sites from France, *Phys. Earth planet. Inter.,* **120,** 111–136.

Constable, C. & Parker, R., 1988. Smoothing, splines and smoothing splines; their application in geomagnetism, *J. Comput. Phys.,* **78,** 493–508.

Day, R., Fuller, M.D. & Schmidt, V.A., 1977. Hysteresis properties of titanomagnetites: grain size and composition dependence, *Phys. Earth planet. Inter.,* **13,** 260–266.

Donadini, F., Korhonen, K., Riisager, P. & Pesonen, L., 2006. Database for Holocene geomagnetic intensity information, *EOS, Trans. Am. geophys. Un.,* **87**(14), 137–143.

Donadini, F., Korte, M. & Constable, C., 2010. Millennial variations of the geomagnetic field: from data recovery to field reconstruction, *Space Sci. Rev.,* **155,** 219–246.

Dunlop, D., 2002. Theory and application of the Day plot (M_{rs}/M_s versus H_{cr}/H_c). 1. Theoretical curves and tests using titanomagnetite data, *J. geophys. Res.,* **107,** doi.:10.1029/2001JB000486.

Green, P. & Silverman, B., 1994. *Nonparametric Regression and Generalized Linear Models: A Roughness Penalty Approach,* Chapman and Hall.

Harrison, R. & Feinberg, J., 2008. FORCinel: an improved algorithm for calculating first-order reversal curve distributions using locally weighted regression smoothing, *Geochem. Geophys. Geosyst.,* **9,** Q05016, doi:10.1029/2008GC001987.

Hervé, G., Chauvin, A. & Lanos, P., 2013. Geomagnetic field variations in Western Europe from 1500BC to 200AD. Part I: directional secular variation curve, *Phys. Earth planet. Int.,* **218,** 1–13.

Jackson, A., 2003. Intense equatorial flux spots on the surface of the Earth's core, *Nature,* **424,** 760–763.

Jackson, A., Jonkers, A. & Walker, M., 2000. Four centuries of geomagnetic secular variation from historical records, *Phil. Trans. R. Soc. Lond. A,* **358,** 957–990.

Jelínek, V., 1981. Characterization of the magnetic fabric of rocks, *Tectonophysics,* **79,** T63–T67.

Kapper, K., Anesin, D., Donadini, F., Angelucci, D., Cavulli, F., Pedrotti, A. & Hirt, A., 2014. Linking site formation processes to magnetic properties. Rock- and archaeomagnetic analysis of the combustion levels at Riparo Gaban (Italy), *J. Archaeol. Sci.,* **41,** 836–855.

Kind, J., 2012. Ferromagnetic resonance spectroscopy and Holocene Earth's magnetic field variations in sedimemnts from Swiss lakes, *PhD thesis,* ETH Zurich, Switzerland.

Kirschvink, J., 1980. The least-squares line and plane and the analysis of paleomagnetic data, *Geophys. J. R. astr. Soc.,* **62,** 699–718.

Koenigsberger, J., 1938. Natural residual magnetism of eruptive rocks, *Terr. Magn. Atmos. Electr.,* **43**(3), 299–320.

Korhonen, K., Donadini, F., Riisager, P. & Pesonen, L., 2008. GEOMAGIA50: an archeointensity database with PHP and MySQL, *Geochem. Geophys. Geosyst.,* **9,** Q04029.

Korte, M., Donadini, C. C.F. & Holme, R., 2011. Reconstructing the Holocene geomagnetic field, *Earth planet. Sci. Lett.,* **312,** 497–505.

Le Borgne, E., 1955. Susceptibilité magnétique anormale du sol superficiel, *Ann. Geophys.,* **11,** 399–419.

Lowrie, W., 1990. Identification of ferromagnetic minerals in a rock by coercivity and unblocking temperature properties, *Geophys. Res. Lett.,* **17**(2), 159–162.

Mauvilly, M., Dafflon, L. & McCullough, F., 2008a. L'abri mésolithique d'Arconciel/La Souche: bilan des recherches 2003–2007, *Cahiers d'Archéologie Fribourgeoise,* **10,** 44–75.

Mauvilly, M., Jeunesse, C. & Doppler, T., 2008b. Ein Tonstempel aus der spätmesolithischen Fundstelle von Arconciel/La Souche (Kanton Freiburg, Schweiz), *Quartär,* **55,** 151–157.

McClean, R. & Kean, W., 1993. Contributions of wood ash magnetism to archaeomagnetic properties of fire pits and hearths, *Earth planet. Sci. Lett.,* **119,** 387–394.

Nielsen, E., 2009. Paläolithikum und Mesolithikum in der Zentralschweiz, Mensch und Umwelt zwischen 17000 und 5500 v. Chr., *Archälogische Schriften Luzern,* **13,** 720 S.

Noel, M. & Batt, C., 1990. A method for correcting geographically remanence directions for the purpose of archaeomagnetic dating, *Geophys. J. Int.,* **102,** 753–756.

Olsen, N. & Stolle, C., 2012. Satellite geomagnetism, *Annu. Rev. Earth Planet. Sci.,* **40,** 441–465.

Panovska, S., Finlay, C., Donadini, F. & Hirt, A., 2012. Spline analysis of Holocene sediment magnetic records: uncertainty estimates for field modeling, *J. geophys. Res.,* **117,** B02101, doi:10.1029/2011JB008813.

Pavón-Carrasco, F.J., Osete, M.L., Torta, J.M. & Gaya-Piqué, L.R., 2009. A regional archaeomagnetic model for Europe for the last 3000 years, SCHA.DIF.3K: applications to archaeomagnetic dating, *Geochem. Geophys. Geosyst.,* **10**(3), Q03013, doi:10.1029/2008GC002244.

Pavón-Carrasco, F.J., Osete, M. & Torta, J., 2010. Regional modeling of the geomagnetic field in Europe from 6000 to 1000 B.C., *Geochem. Geophys. Geosyst.,* **11**(11), 20, Q11008, doi:10.1029/2010GC003197.

Pike, C., Roberts, A. & Verosub, K., 2001. First-order reversal curve diagrams and thermal relaxation effects in magnetic particles, *Geophys. J. Int.,* **145,** 721–730.

Pinto Jr, O., Gonzalez, W., Pinto, I., Gonzalez, A. & Jr, O.M., 1992. The south atlantic magnetic anomaly: three decades of research, *J. Atmos. Terr. Phys.,* **54**(9), 1129–1134.

Reimer, P.J. *et al.*, 2009. IntCal09 and Marine09 radiocarbon age calibration curves, 0-50,000 years cal BP, *Radiocarbon,* **51**(4), 1111–1150.

Roberts, A. & Winklhofer, M., 2004. Why are geomagnetic excursions not always recorded in sediments? Constraints from post–depositional remanent magnetization in lock–in modeling, *Earth planet. Sci. Lett.,* **227,** 345–359.

Roberts, A., Pike, C. & Verosub, K., 2000. First–order reversal curve diagrams: a new tool for characterizing the magnetic properties of natural samples, *J. geophys. Res.,* **105**(B12), 28 461–28 475.

Snowball, I., Zillén, L., Ojala, A., Saarinen, T. & Sandgren, P., 2007. FENNOSTACK and FENNORPIS: varve dated holocene palaeomagnetic secular variation and relative palaeointensity stack for Fennoscandia, *Earth planet. Sci. Lett.,* **255,** 106–116.

Tauxe, L., 1998. *Paleomagnetic Principles and Practice,* Kluwer.

Tauxe, L., Butler, R., Banerjee, S. & van der Voo, R., 2010. *Essentials of Paleomagnetism,* University of California Press.

Tema, E. & Kondopoulou, D., 2011. Secular variation of the Earths magnetic field in the Balkan region during the last eight millennia based on archaeomagnetic data, *Geophys. J. Int.,* **186,** 603–614.

Turner, G. & Thompson, R., 1981. Lake sediment reord of the geomagnetic secular variation in Britain during Holocene times, *Geophys. J. R. astr. Soc.,* **65,** 703–725.

Turner, G. & Thompson, R., 1982. Detransformation of the british geomagnetic secular variation record for holocene times, *Geophys. J. R. astr. Soc.,* **70,** 789–792.

Verosub, K., 1997. Depositional and postdepositional processes in the magnetization of sediments, *Rev. Geophys.,* **15**(2), 129–143.

Vigliotti, L., 2006. Secular variation record of the Earth's magnetic field in Italy during the Holocene: constraints for the construction of a master curve, *Geophys. J. Int.,* **165,** 414–429.

Walker, M. & Jackson, A., 2000. Robust modelling of the earth's magnetic field, *Geophys. J. Int.,* **143,** 799–808.

Zijderveld, J., 1967. *A.C. Demagnetization in Rocks: Analysis of Results,* pp. 254–286, Elsevier.